



Contents lists available at ScienceDirect

Radiation Physics and Chemistry

journal homepage: www.elsevier.com/locate/radphyschem

Perforated diode neutron detector modules fabricated from high-purity silicon

D.S. McGregor^{a,*}, S.L. Bellinger^a, D. Bruno^a, W.L. Dunn^b, W.J. McNeil^a, E. Patterson^a, B.B. Rice^a, J.K. Shultis^b, T. Unruh^a^a S.M.A.R.T. Laboratory, Department of Mechanical and Nuclear Engineering, 3002 Rathbone Hall, Kansas State University, Manhattan, KS 66506-2503, USA^b Department of Mechanical and Nuclear Engineering, 3002 Rathbone Hall, Kansas State University, Manhattan, KS 66506-2503, USA

ARTICLE INFO

PACS:
29.40.WkKeywords:
Semiconductor neutron detectors
Perforated detectors
Perforated diodes

ABSTRACT

Compact neutron detectors are being designed and tested for use as low-power real-time personnel dosimeters. The neutron detectors are *pin* diodes that are mass produced from high-purity Si wafers. Each detector has thousands of circular perforations etched vertically into the device. The perforations are backfilled with ⁶LiF to make the *pin* diodes sensitive to thermal neutrons. The prototype devices deliver 4.7% thermal neutron detection efficiency while operating on only 15 V, showing a 9% increase in efficiency over identical planar devices.

© 2009 Published by Elsevier Ltd.

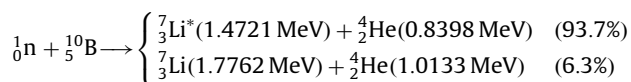
1. Introduction

Semiconductor radiation detectors composed of diode devices coated with neutron reactive films have been studied for decades (Neutron Detectors, 1966). Material choice requires a strong neutron absorbing reactive coating that emits ionizing reaction products, preferably charged particles rather than photons. There are many strong neutron absorbers with large absorption cross sections, yet only a few of these choices spontaneously emit ionizing radiation in the form of charged particles. Typically, the neutron reactive material covering the diodes is natural Gd, ¹⁰B or ⁶LiF.

The thermal neutron (2200 ms⁻¹) capture cross section for ¹⁵⁷Gd is 240,000 barns, which permits efficient absorption of thermal neutrons in a thin film of material. Natural Gd, which has a ¹⁵⁷Gd natural abundance of 15.7%, has a thermal neutron capture cross section of 46,000 barns. However, only 60% of thermal neutron captures result in the release of a conversion electron, which reduces the effective thermal cross section of natural Gd to 27,600 barns. The (n,γ) reactions yield numerous low energy conversion electrons, with a general distribution ranging from 29 up to 246 keV (Schulte et al., 1994). However, the largest yields are from conversion electrons with energies near 70 keV, with all other energy emissions above 85 keV having much lower branching efficiencies (Schulte et al., 1994). As a result, the reaction products from Gd are mostly low energy conversion

electrons, which can be easily confused with background gamma ray or beta particle interactions. For this reason, Gd coatings are generally not used as a converter for coated semiconductor neutron detectors.

The ¹⁰B(n,α)⁷Li neutron reaction yields two possible decay branches from the excited ¹¹B compound nucleus, namely



where the Li ion in the 94% branch is ejected in an excited state, which deexcites through the emission of a 480 keV gamma ray. For thermal neutrons, the two charged-particle reaction products are ejected in opposite directions. Fully enriched ¹⁰B has a microscopic absorption cross section for thermal neutrons of 3840 barns. With a mass density of 2.15 g cm⁻³, the solid structure of ¹⁰B has a macroscopic thermal absorption cross section of 500 cm⁻¹. The absorption cross section for ¹⁰B follows a 1/v dependence (Garber and Kinsey, 1976; McLane et al., 1988). ¹⁰B has been used successfully as a neutron conversion mechanism on semiconductor diodes for over 45 years, and has been used in the first demonstration of perforated diode structures (McGregor et al., 2002).

The ⁶Li(n,t)⁴He neutron reaction yields a single product branch,



For thermal neutrons, the charged-particle reaction products are ejected in opposite directions. The reaction products from the ⁶Li(n,t)⁴He reaction are more energetic than those of the

* Corresponding author. Fax: +1785 532 7057.

E-mail address: mcgregor@ksu.edu (D.S. McGregor).URL: <http://www.mne.ksu.edu/research/centers/SMARTlab> (D.S. McGregor).

$^{10}\text{B}(n, \alpha)^7\text{Li}$ or $^{157}\text{Gd}(n, \gamma)^{158}\text{Gd}$ reactions and, hence, are much easier to detect and discriminate from background radiations. ^6Li has a relatively large microscopic thermal neutron absorption cross section of 940 barns, although it is less than ^{157}Gd and ^{10}B . The absorption cross section for ^6Li follows a $1/v$ dependence (Garber and Kinsey, 1976; McLane et al., 1988). Although devices have been fabricated with enriched ^6Li metal as the converter film (McGregor et al., 2003), pure Li is highly reactive and difficult to prevent from decomposing, even when using encapsulates. It is the stable compound LiF that is used more often. The mass density of ^6LiF is 2.54 g cm^{-3} , and the resulting macroscopic thermal neutron absorption cross section is 57.5 cm^{-1} .

The advantages of coated diodes as neutron detectors include compact size, a low power requirement, low cost VLSI mass production methodology, and ruggedness. Yet, since basic planar thin-film-coated diode detectors can only achieve practical maximum thermal neutron detection efficiencies of approximately 4.5% (McGregor et al., 2003), they have experienced only modest utilization as neutron radiation detectors. Recent advances with high-aspect ratio deep etching (HARDE) techniques have allowed for unique perforated neutron detector structures to be realized. Under such a configuration, the diode is permeated with perforations which are backfilled with neutron reactive materials, such as ^{10}B and ^6LiF . As a result, the intrinsic thermal neutron detection efficiencies of perforated diodes can be increased above 25%, more than 5 times that of a common planar thin-film-coated diode (Shultis and McGregor, 2006). It was shown in previous work that perforated devices incorporating ^6LiF as the converter can achieve higher intrinsic thermal neutron detection efficiencies than devices with ^{10}B as the converter (Shultis and McGregor, 2006). Hence, of the three main materials commonly used for thin-film-coated thermal neutron detectors, the following work concentrates on devices constructed with only ^6LiF as the converter material.

2. Theoretical considerations

Monte Carlo simulations have been used to predict the performance of a perforated diode as a function of absorber material, hole diameter and depth, hole pitch, and “cap” layer thickness (Shultis and McGregor, 2006). A parallel neutron beam, perpendicular to the detector face, is assumed to uniformly illuminate the detector face. The silicon semiconductor is assumed transparent to these neutrons and the total cross section for the converter material is taken as the ion-producing cross section. Neutron scattering effects in the Si substrate are negligible and are not considered. The notations for a perforated diode unit cell are shown in Fig. 1. The square unit cell containing a central cylindrical hole is replicated many times in the x and y directions to compose an entire detector. However, the simulation needs to consider only a single unit cell to determine the spectral features of the energy deposited in the semiconductor material and the resulting neutron detection efficiency. The basic method is described in the literature (McGregor and Shultis, 2004).

2.1. Monte Carlo simulations of ion energy depositions

By sampling uniformly over the illuminated surface of the detector, a random point (x_i, y_i) for a neutron incident on the detector surface is determined. Then along a ray through this entry point, a random depth z_i for a neutron interaction in the converter material is obtained by sampling from the distribution $f(z) = C \exp(-\Sigma z)$ where Σ is the thermal-averaged macroscopic cross section for the converter material. Here $C = \Sigma[1 - \exp(-\Sigma T)]^{-1}$ is a normalization constant to make $f(z)$ a properly

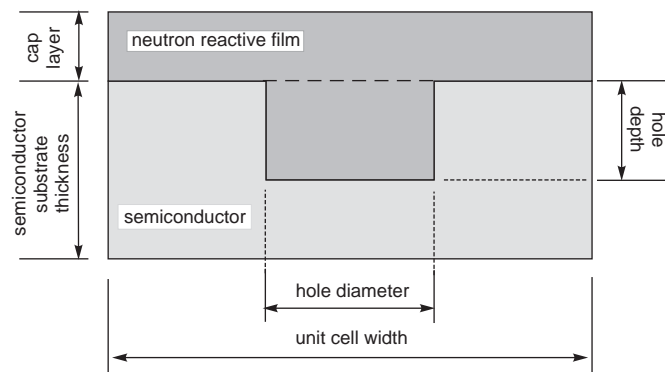


Fig. 1. Notations for a square perforated diode unit cell. The x - and y -axes are in the plane and parallel to the sides of the square cap top and the z -axis is raised through the central hole axis from bottom to top.

normalized probability density function (pdf). The depth T is the length of the ray through the converter material. If no converter material is in the path of the neutron ray ($T = 0$) then the neutron passes through the detector without interaction. Once a random interaction site (x_i, y_i, z_i) is determined, a random direction $\Omega_i = (u_i, v_i, w_i)$, where (u_i, v_i, w_i) are the direction cosines for Ω_i , for one of the ions is selected from an isotropic directional distribution. The other reaction ion is then given the opposite direction $(-u_i, -v_i, -w_i)$. Finally, the identity of the ions is randomly selected according to the branching ratio of the various ions produced in the neutron interaction. The two ions are then tracked along their paths in the detector, and the energy transferred to the silicon semiconductor regions is calculated.

The estimation of the energy deposited in various regions of a silicon semiconductor detector by ions produced by thermal neutron reactions in adjacent regions of boron or lithium fluoride is greatly simplified if all ions are assumed to travel in straight lines, i.e., scattering events and energy straggling can be neglected. For the energies of the ions considered here, a straight-line slowing-down trajectory is a good approximation (Shultis and Faw, 2000). Calculation of the energy deposited in the various regions of the detector is then simply a matter of computing the length of the geometric segments an ion travels in each material encountered along its straight-line path from the ion's point of birth to where it is stopped. The energy deposited in the silicon by each simulated ion history is then found by calculating the energy lost by the ion over every path segment it travels in the silicon.

The energy deposited in the silicon, E_d , for a given path segment depends on the length s of the straight-line path segment in the silicon, the ion type i , and the ion-energy upon entering the silicon E . Such a function $E_d^i(E, s)$ is complicated and generally not known. Here a novel and simpler back-tracking method is presented that requires far simpler empirical functions.

To calculate the energy lost by an ion over each of its path segments by the back-tracking method, two empirical functions are needed. The first $E_m^i(s)$ is the mean residual energy after an ion of type i travels a distance s in material m from its point of birth. To obtain this function, the TRIM code (Ziegler and Biersack, 2003) was used to obtain a detailed tabulation of the mean residual energy of the various ions produced by thermal neutron interactions in the converter material (^6LiF or ^{10}B) as a function of path length in the converter material and in silicon. Then the TableCurve (Jandel Scientific, 1991) computer program was used to find an empirical fit to these data. In this way accurate empirical formulas were found for $E_m^i(s)$ that permitted rapid evaluation of an ion's residual energy. The second function needed for the present Monte Carlo calculations is $S_m^i(E)$, which gives the

path length in material m for the i th ion to obtain a mean residual energy E . This function is the inverse of $E_m^i(s)$. With the previous TRIM data, empirical fits for $S_m^i(E)$ were obtained. The function $S_m^i(E)$ also gives the mean range R_m^i of the i th ion in material m , namely $R_m^i = S_m^i(0)$. Also if $s > R_m^i$ then $E_m^i(s) = 0$. With these two empirical fits for $E_m^i(s)$ and $S_m^i(E)$, the energy deposited by an ion along any straight-line segment in any of the detector regions can readily be obtained.

Consider an ion that leaves a region composed of material 1 with energy E_1 and enters an adjacent region composed of material 2. The ray in the direction of the ion travel is assumed to have a segment length s_2 in the second region, i.e., the distance from the point where the ion enters the second region to the point where the ray intersects another region, the detector boundary, or is stopped. The problem is to estimate the energy deposited along s_2 and the residual ion energy E_2 (if any) at the end of its path in the second region. Clearly, if the ion with an initial energy E_1 in material 2 has a range less than s_2 , the energy deposited in the second region is $E_d = E_1$ since $E_2 = 0$. However, if this range is greater than s_2 , then $E_2 > 0$ and the deposited energy is $E_d = E_1 - E_2$.

To calculate E_2 at the end of the ray in the second medium, the trajectory is first tracked backwards to find the ion's starting position, if the material of the regions traversed by the ion before entering the second region were replaced by the material of the second medium, that would produce the same residual energy E_1 at the interface. This back-tracked distance is $s_1 = S_2^i(E_1)$. The energy E_2 after a path length $s_1 + s_2$, all in the material of medium 2, is simply $E_2 = E_1^i(s_1 + s_2)$. In this manner the energy deposited along the path segment s_2 is evaluated as $E_d = E_1 - E_2$. The same approach can be used to evaluate the energy lost by the ion over any path segment.

The energy the two reaction ions deposit in the silicon regions along their tracks is then recorded in an appropriate bin or tally vector for each simulated reaction event. After performing this simulation for several million reactions, an ideal energy-deposition spectrum is thus obtained. Further, the fraction of neutron histories that deposited energy greater than some minimal amount E_{cut} gives the detector efficiency for producing a pulse greater than E_{cut} .

2.2. Simulation of measured spectra

The spectra obtained by Monte Carlo simulations described above are ideal in the sense that no energy straggling, large-angle ion scattering or detector noise and resolution effects are considered. To simulate expected multi-channel analyzer measured spectra, which include such non-ideal effects, the ideal spectra are post processed to introduce a Gaussian averaging or smearing of the counts in each energy bin of the ideal spectra (McGregor and Shultis, 2004).

Let $P(E)dE$ be the probability a neutron reaction leads to the deposition of energy in dE about E . The number of counts N_i in channel i of the ideal spectrum is

$$N_i = N_{tot} \int_{E_i - \Delta}^{E_i + \Delta} P(E) dE \simeq 2\Delta N_{tot} P(E_i), \quad (1)$$

where E_i is the channel midpoint energy, 2Δ is the bin energy width, and N_{tot} is the total number of simulated neutron reactions. Because of non-ideal effects, an energy deposition of E has a probability $\mathfrak{R}(E, E') dE'$ of being recorded in dE' about E' . To a first approximation, a Gaussian resolution function is assumed, i.e.,

$$\mathfrak{R}(E, E') = \frac{1}{\sqrt{2\pi}\sigma} \exp\left[-\frac{1}{2}\left(\frac{E - E'}{\sigma}\right)^2\right]. \quad (2)$$

The probability a reaction that deposits energy in dE about E and is then recorded in channel j of the MCA spectrum is thus

$$C_j(E) dE = P(E) dE \int_{E_j - \Delta}^{E_j + \Delta} \mathfrak{R}(E, E') dE', \quad (3)$$

so that the number of counts in channel j of the measured spectrum is

$$\begin{aligned} N_j &= N_{tot} \int_0^{E_{max}} C_j(E) dE \\ &= N_{tot} \int_0^{E_{max}} P(E) \left[\int_{E_j - \Delta}^{E_j + \Delta} \mathfrak{R}(E, E') dE' \right] dE \\ &\simeq N_{tot} \sum_{i=1}^{N_{max}} P(E_i) 2\Delta \left[\int_{E_j - \Delta}^{E_j + \Delta} \mathfrak{R}(E_i, E') dE' \right] \\ &= \sum_{i=1}^{N_{max}} N_i W_{ij}, \end{aligned} \quad (4)$$

where E_{max} is the maximum spectral energy, N_{max} is the maximum number of MCA energy bins, and the spreading vector is

$$\begin{aligned} W_{ij} &= W_{ji} = W_{|i-j|} \equiv \frac{1}{\sqrt{2\pi}\sigma} \int_{E_j - \Delta}^{E_j + \Delta} \exp\left[-\frac{1}{2}\left(\frac{E_i - E'}{\sigma}\right)^2\right] dE' \\ &= \frac{1}{2} \left\{ \operatorname{erf}\left(\frac{E_j + \Delta - E_i}{\sqrt{2}\sigma}\right) - \operatorname{erf}\left(\frac{E_j - \Delta - E_i}{\sqrt{2}\sigma}\right) \right\}. \end{aligned} \quad (5)$$

The devices used in the present study were fabricated with 30 μm diameter holes, each 20 μm deep, inside square unit cells with 60 μm sides. The calculated spectrum from such a device, backfilled with ${}^6\text{LiF}$ and with a 10 μm thick ${}^6\text{LiF}$ cap layer, is shown in Fig. 2. There are certain spectral features that appear in the perforated diode spectrum that will not appear in the spectrum of a common thin-film-coated diode. First, there is a clear spectral cut off at an energy of 2.73 MeV, which corresponds to the maximum energy that a single particle from the ${}^6\text{Li}(n, t){}^4\text{He}$ neutron reaction can deposit in the device. This same feature appears as an end-point energy for a planar device. Second, there is the dual-particle spectrum beyond 2.73 MeV, which is a continuum of energies resulting from both particles depositing energy in the detector from a single reaction event in the holes. For thermal neutrons, the dual-particle continuum is possible only in the perforated design. For the specified detector perforation dimensions and pitch, the maximum possible intrinsic thermal neutron detection efficiency for the device is

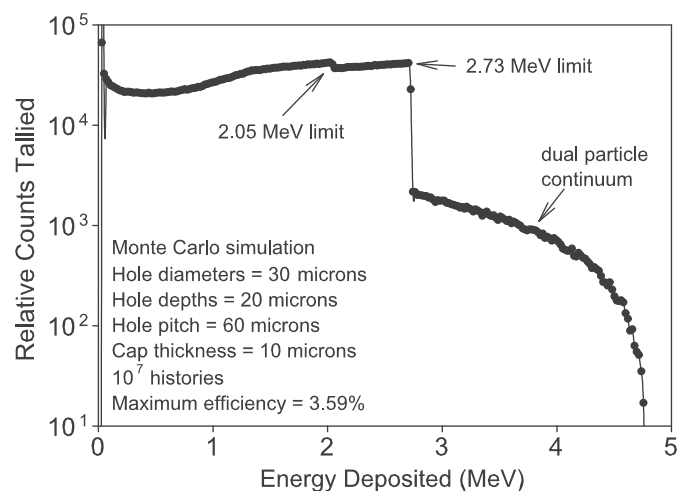


Fig. 2. The calculated spectrum from a perforated Si device having 30 μm -diameter holes, each 20 μm deep, filled with ${}^6\text{LiF}$. A final 10 μm thick ${}^6\text{LiF}$ cap layer covers the device. The device hole pitch was 60 μm . For this simulated spectrum a standard deviation of $\sigma = 20$ keV, typical of silicon detectors, was assumed.

only 3.59%. However, an efficiency of only 2.95% is achievable with a common planar thin-film-coated diode with a 10 μm thick ^6LiF cap. Hence, the thermal neutron detection efficiency should increase from 2.95% to 3.59% by using a perforated detector over a planar detector. A calculation conducted for the same configuration, except with a 22 μm cap layer, indicated that the perforated device would yield 5.41% thermal neutron detection efficiency as compared to only 4.5% for a planar device with the same coating thickness. Much higher efficiencies can be achieved with deeper holes (Shultis and McGregor, 2006).

3. Device design and fabrication

The first-generation deep-perforation diode designs were produced as Si *pin* diode detectors. The diode fabrication processes were carried out on 3-in. diameter float zone, double-side polished, > 10,000 Ωcm , n-type TopSil wafers approximately 325 μm thick. The wafers were cleaned with a two-step wet-chemical process consisting of a 5-min Piranha etch at 120 $^\circ\text{C}$ followed by a 5-min Baker Clean : H_2O_2 : H_2O (5:1:25) etch at 70 $^\circ\text{C}$. Both steps were followed by a 30-s de-ionized (DI) water:buffered oxide etch (6:1). The wafers were rinsed in a DI water cascade for at least 1 min.

A thick thermally grown SiO_2 layer was generated to provide both a diffusion mask and electrical isolation between die on the wafer. The backside oxide of the wafers was stripped and n-type junctions were diffused into the back to produce ohmic contacts. A second oxidation step was performed to protect the n-type ohmic contact junctions. Then photolithography was used to define 5.6-mm diameter circular junction regions on the front of the wafer. Within these circular regions, 42- μm diameter circular oxide dots were defined to prevent dopant introduction into the perforation sites. Shallow p-type regions were diffused into the surface leaving behind, including effects from sideways diffusion, 38- μm diameter undoped circular regions arranged in a 60- μm center-to-center matrix over the entire 5.6-mm diameter p-type junction.

Photolithography was used to define 30- μm diameter open regions aligned and centered over the 38- μm diameter undoped regions in the 5.6-mm diameter p-type circular rectifying junctions. The 30- μm diameter openings are used for the perforation etching step. Hence, the etched holes will not punch directly through the *pin* junction region, which could otherwise degrade the quality of the rectifying barrier. An Oxford Plasmalab System 100 was used to etch holes 20 μm deep into the Si substrate through the 30- μm diameter photoresist openings. Although the system has been used to etch holes up to 300 μm deep, the first-generation devices were constructed with only 20 μm deep holes (Fig. 3). Next, a final oxidation step was performed to insulate the hole interiors from damage that might occur during the LiF filling process. Photolithography was used to define annuli perimeters around the p-type pad regions. Then liftoff was used to fabricate conductive contacts within the annuli on the p-type regions, where a 250 \AA layer of Ti followed by a 2500 \AA layer of Au were evaporated over the substrate. Lastly, the backside n-type region was coated with 250 \AA of Ti followed by 2500 \AA of Au.

^6LiF was produced through a simple two-step chemical reaction. Small pieces of 95.5% enriched ^6Li metal were placed into 500 ml of DI water to make a $^6\text{LiOH}$ solution. ^6Li pieces were added until the solution became saturated. Then a dilute solution of HF was titrated into the $^6\text{LiOH}$ solution to produce ^6LiF , which appeared as a white powder accumulating at the bottom of the beaker. During the titration process, the $^6\text{LiOH}$ solution was constantly stirred. The process was continued until a pH between

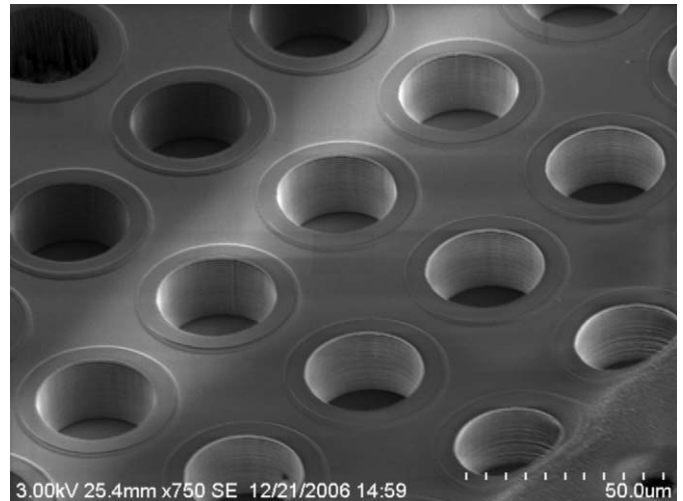


Fig. 3. Perforations are etched into the Si substrate with ICP-RIE. Shown are holes etched into Si, each 30 μm in diameter and 20 μm deep on a center-to-center pitch of 60 μm .

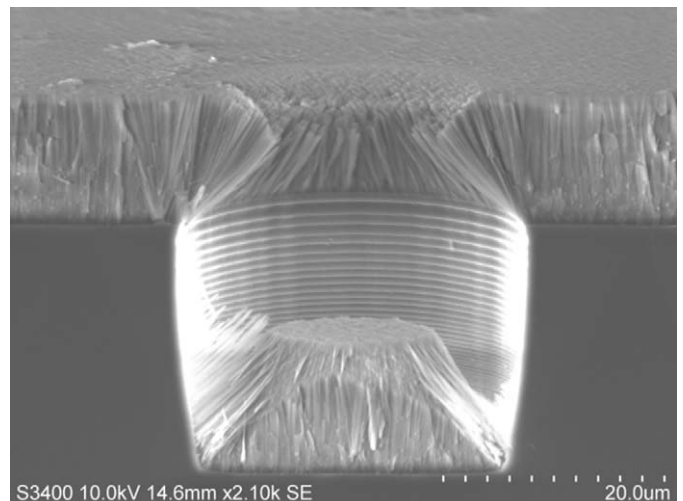


Fig. 4. ^6LiF film, 10.8 μm thick, evaporated into a 30- μm diameter by 20 μm deep hole. Notice that the ^6LiF is closing the hole, thereby creating a region devoid of absorber material.

6.8 and 7.2 was reached. The ^6LiF powder was then filtered and dried in an oven. On the initial samples, ^6LiF was deposited through physical vapor deposition, which unfortunately did not completely fill the holes. Similar to difficulties experienced with ^{10}B (McGregor et al., 2002), the ^6LiF closed the hole and limited the amount of material that could be deposited in the hole (Fig. 4). To prevent void formation, many devices were backfilled by gently pressing the ^6LiF powder material into the holes (Fig. 5). Afterwards, a ^6LiF cap layer was deposited atop the device with physical vapor deposition (Fig. 6), ranging from 10.8 μm on some devices to 22 μm on others.

4. Module design

First-generation perforated detectors were coupled to a simple counting system with a small low cost and low-power transimpedance and gain amplifier combination. The amplifiers and detection diode are located in a sealed 4 pin (14 pin footprint) package widely used in the manufacture of crystal oscillators. The

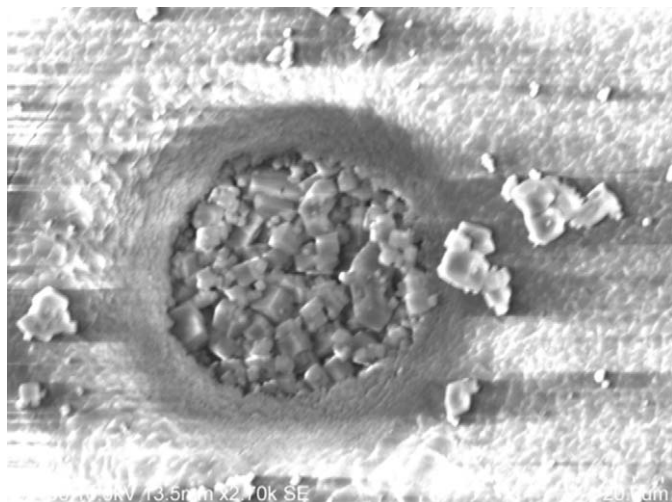


Fig. 5. ^6LiF powder material physically pressed into a 30- μm diameter by 20 μm deep hole.

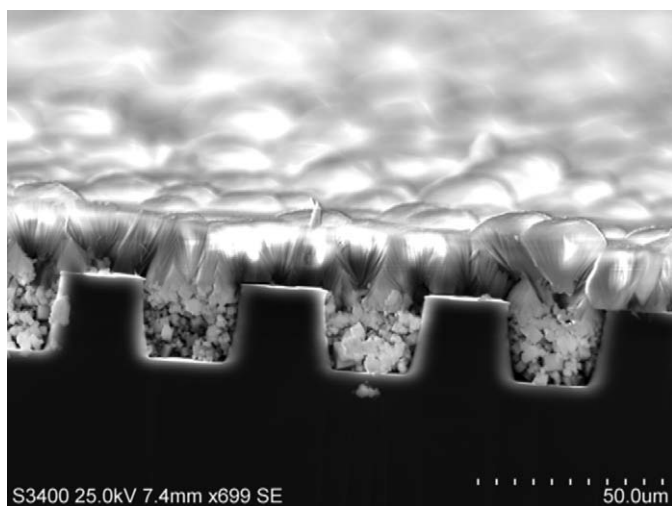


Fig. 6. ^6LiF powder material physically pressed in 30- μm diameter by 20 μm deep holes with an evaporated ^6LiF cap film.

wire bonds between the diode and the transimpedance amplifier are also potted in an electronics grade epoxy to ensure stability. Once packaged, the diode “module” is well shielded from external light, electrical noise, and humidity. The module supplies power for the amplifier and perforated detector bias (nominally around 15 V), and returns a positive polarity pulse output from neutron interactions between 70 and 130 mV with a $\approx 4\text{-}\mu\text{s}$ pulse width (depending on the individual diode). The module requires an operating voltage between 2.7 and 5 V at 150 μA . The bias supply uses a charge pump circuit with an external adjustment potentiometer to supply between 10 and 20 V of positive detector bias. It is based on a LT1615-1 DC/DC step up converter. The bias supply is also contained in a 4-pin crystal carrier for noise isolation (Figs. 7–11).

Pulses exiting the amplifier circuit are converted into a logic-level pulse for the counting circuits. An adjustable voltage discrimination level is set with a potentiometer and connected to the negative input of a low-power comparator. The pulse is connected to the non-inverting input of the comparator with an RC filter to remove a small dc offset introduced by the amplification stage. This allows the device to “discriminate” pulse heights, as well as filter out spurious noise. The prototype

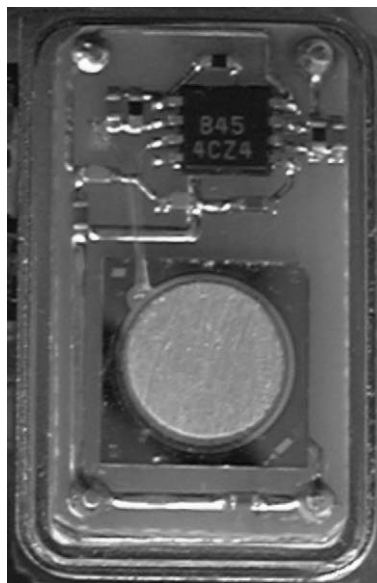


Fig. 7. Perforated detector and preamplifier circuit.

arrangement operates on 3 AAA cell batteries (4.5 V), and uses a low-power commercial counter to display neutron induced counts. The unit is constructed using surface mount components and techniques, and is housed in an aluminum box. Module testing was initially performed with an ^{241}Am alpha-particle source. The aluminum housing has a hole drilled above the perforated detector covered by an aluminized mylar window. The hole allows the 5.5 MeV alpha particles to enter the detector and produce pulses.

5. Characterization and results

5.1. IV and CV measurements

The prototype diodes were tested for IV and CV characteristics, shown in Figs. 12 and 13. From Fig. 12, the leakage current for the perforated diodes was measured to be 200 nA at a reverse bias of 35 V. From Fig. 13, a bias voltage of 35 V coincides with the voltage necessary to achieve full depletion of the device. Higher applied voltage only increased the leakage current without any appreciable reduction in the device capacitance. Overall, the IV and CV measurements indicate the regions around the holes are depleted and active, as needed for the perforated device concept to operate properly.

The device modules were tested, with an ^{241}Am α -particle source, for pulse width and pulse height as a function of bias voltage. The results are shown in Fig. 14. The pulse widths, on average, leveled off at approximately 3.7 μs beyond 15 V bias. The pulse height leveled off in magnitude at approximately 130 mV for voltages exceeding 10 V bias. Because the depletion region need only extend an equivalent distance to that of the triton range beyond the overall perforation depth (approximately 30 μm beyond the hole depth) to produce full charge collection, the voltage needed for optimum operation is actually less than needed for full depletion, speculated to be 35 V from Fig. 13.

5.2. Thermal neutron measurements

The devices were tested in a tangential thermal beamport at the Kansas State University's TRIGA Mark II Nuclear Reactor Facility. The spectral features from the devices that were

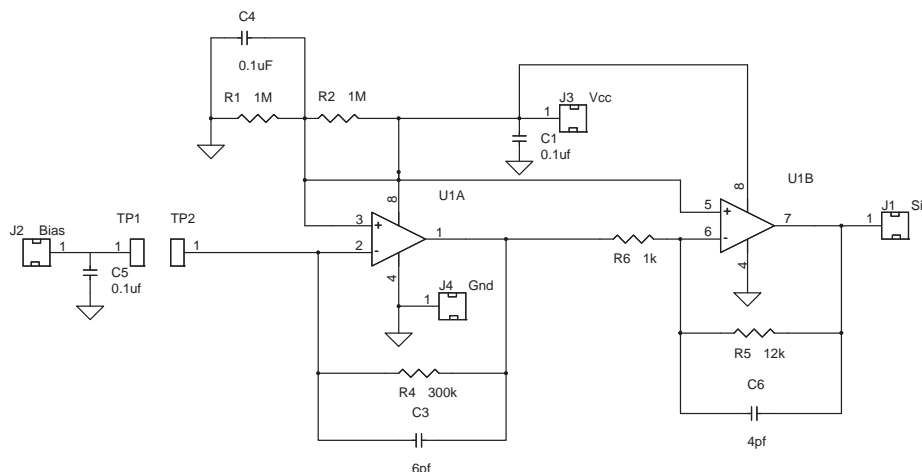


Fig. 8. Preamplifier circuit design.

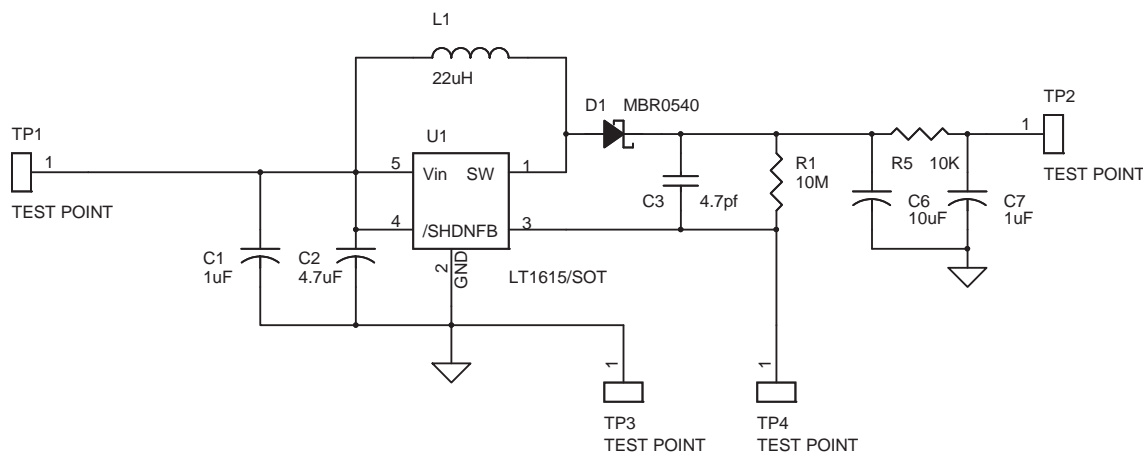


Fig. 9. Bias supply circuit design.

backfilled by physical vapor deposition (Fig. 4) are shown in Fig. 15. Notice that the salient spectral features expected from a perforated device are present, namely the 2.73 MeV triton reaction product limit and the dual-particle continuum. A second continuum of counts beyond the dual-particle continuum is from pulse pileup, as seen in Fig. 15. Due to the void regions in the perforations, efficiency comparisons were not made.

Calibration detectors designed as simple planar diodes were used to determine the thermal neutron flux. The calibration detectors were *pin* diodes coated with 1400 Å of 95.5% enriched ⁶LiF, each having a thermal neutron detection efficiency of 0.076%. To reduce effects from pulse pileup, the perforated detectors were tested with the reactor power at 200 W. The beam calibration yielded an average thermal neutron flux of 228 n cm⁻² s⁻¹ at the detector plane for a reactor power of 200 W. The perforated diodes had 30 μm diameter holes that were 20 μm deep.

As previously described, the holes were backfilled with pressed ⁶LiF powder, thereby reducing void regions. For comparison purposes, basic planar Si diode detectors were fabricated alongside the perforated diodes. A final 22 μm thick cap layer of ⁶LiF was vapor deposited over both the planar and perforated diodes during the same deposition run.

Both the planar and perforated detectors were tested in the same electronics box under identical conditions. The reactor power was maintained at 200 W for all measurements. For each detector tested, a spectrum was accumulated with the detector exposed directly in the thermalized neutron beam and another

spectrum was accumulated with a 1 mm thick Cd shield placed between the beam port and the detector. The Cd sheet was placed at the beam port exit several feet away from the detector to ensure that prompt activation gamma rays did not add to the background. The difference between the two spectra yields the net neutron induced counts (see Fig. 16). The net counts accumulated from the *planar* device in a period of 20 min were 2974 ± 54.5, corresponding to a count rate of 2.48 ± 0.05 cps. With an active detector area of 25 mm², the calculated thermal neutron detection efficiency of the device was 4.35 ± 0.08%. The net counts accumulated from the *perforated* device in a period of 20 min were 3202 ± 56.6, corresponding to a count rate of 2.67 ± 0.05 cps. With an active detector area of 25 mm², the calculated thermal neutron detection efficiency of the device was 4.7 ± 0.083%. Hence, the perforated device is yielding higher efficiencies than a simple planar diode counterpart. By comparison, after correcting for 95.5% enriched ⁶LiF, the planar device was expected to yield 4.31% efficiency and the perforated device was expected to yield 5.17% efficiency.

6. Conclusions and future work

Si-based perforated diode detectors have been fabricated and demonstrated in compact low-power packages. The perforated devices have yielded approximately 4.7 ± 0.083% thermal neutron detection efficiency, as compared to an expected value of only

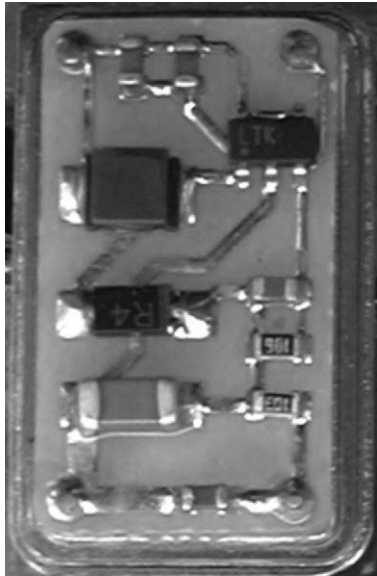


Fig. 10. Bias supply for the detector.

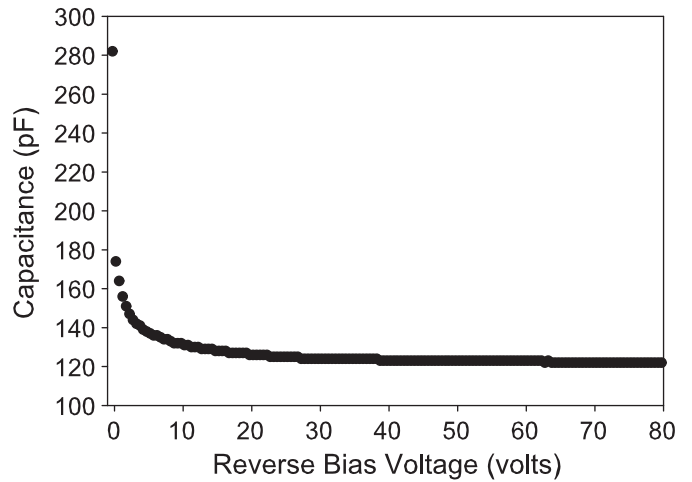


Fig. 13. Capacitance–voltage plot indicating deep depletion at reverse bias voltages above 35 V.

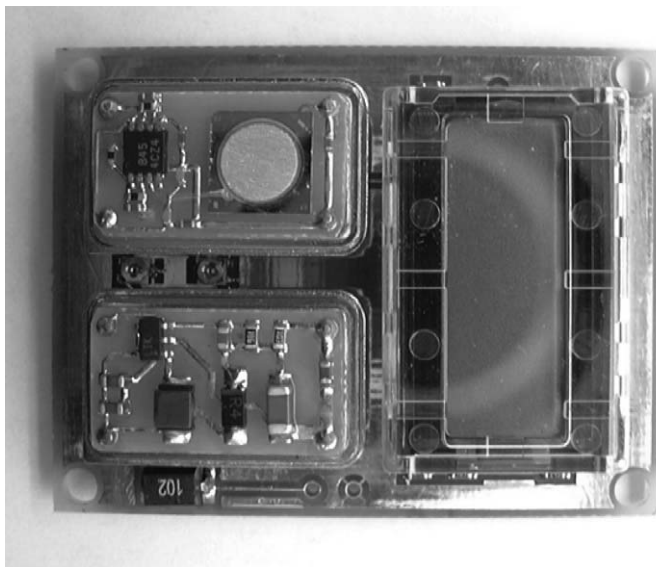


Fig. 11. Compact module showing the detector and related circuits.

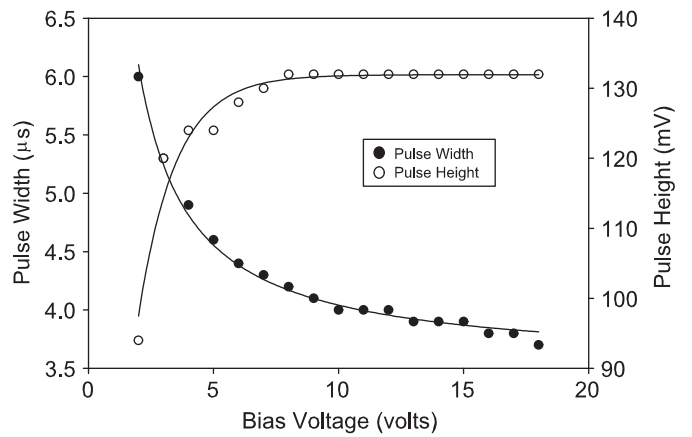


Fig. 14. Output pulses from 5.5 MeV ^{241}Am alpha particles should be 5.5 MeV ^{241}Am , showing the change in pulse height and pulse width as a function of detector bias voltage.

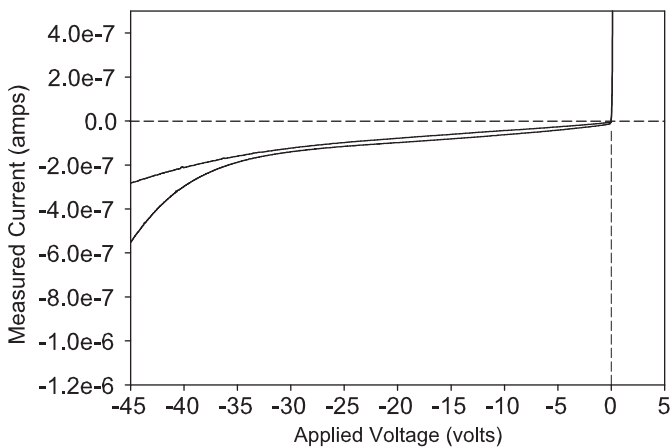


Fig. 12. Current–voltage plot indicating deep depletion.

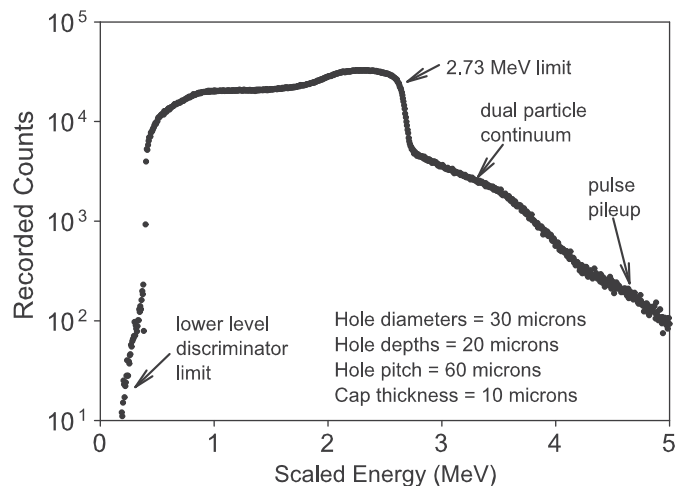


Fig. 15. A spectrum from a perforated Si device having 30 μm diameter holes, each 20 μm deep, backfilled with ^6LiF powder. The device was covered with a 10.8 micron thick ^6LiF layer. The device hole pitch is 60 μm . The major expected spectral features are clearly visible.

4.31% for a planar device and 5.17% for a perforated device, both of the same dimensions. The lower observed efficiency, as compared to the expected modeled efficiency, may be due, in part, to

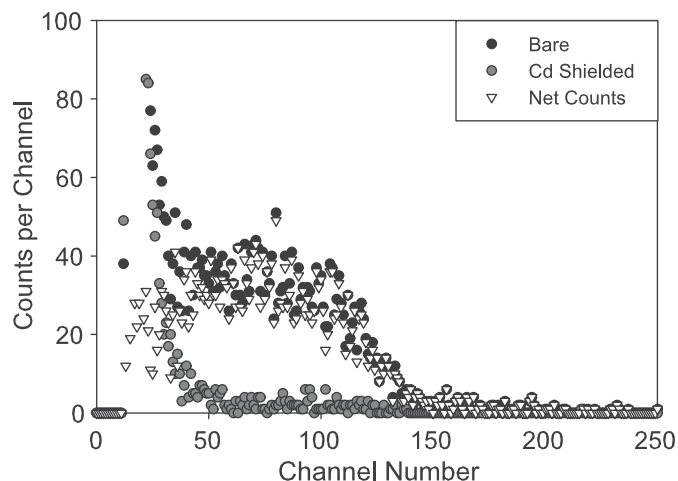


Fig. 16. Neutron induced spectra from a perforated Si device having $30\ \mu\text{m}$ diameter holes, each $20\ \mu\text{m}$ deep, backfilled with ^6LiF powder. The device has a $22\ \mu\text{m}$ thick ^6LiF cap overlayer. The device hole pitch is $60\ \mu\text{m}$. Shown are total, background and net spectra from the device.

incomplete ^6LiF powder packing in the holes, where void space is still present, as can be seen in Fig. 6. Regardless, efficiency improvement over a planar design with the same dimensions and ^6LiF cap layer has been demonstrated. Further, the major spectral features expected from perforated diode structures were observed. Future generation devices will be constructed from diodes with much deeper perforations and a tighter perforation matrix. Both changes will increase the intrinsic thermal neutron detection efficiency.

Acknowledgments

This work was supported under DTRA Contract DTRA-01-03-C-0051, National Science Foundation IMR-MIP Grant no. 0412208, and US Department of Energy NEER Grant DE-FG07-04ID14599.

References

- Garber, D.I., Kinsey, R.R., 1976. BNL 325: Neutron Cross Sections. Curves, vol. 2, third ed. Brookhaven National Laboratory, Upton.
- Jandel Scientific, 1991. Table Curve, version 3.0, Curve Fitting Software, Jandel Scientific, Corte Madera, CA.
- McGregor, D.S., Shultis, J.K., 2004. Spectral identification of thin-film-coated and solid-form semiconductor neutron detectors. Nuclear Instruments and Methods A 517, 180–188.
- McGregor, D.S., Klann, R.T., Gersch, H.K., Ariesanti, E., Sanders, J.D., Van Der Elzen, B., 2002. New surface morphology for low stress thin-film-coated thermal-neutron detectors. IEEE Transactions on Nuclear Science 49, 1999–2004.
- McGregor, D.S., Hammig, M.D., Gersch, H.K., Yang, Y.-H., Klann, R.T., 2003. Design considerations for thin film coated semiconductor thermal neutron detectors, part I: basics regarding alpha particle emitting neutron reactive films. Nuclear Instruments and Methods A 500, 272–308.
- McLane, V., Dunford, C.L., Rose, P.F., 1988. In: Neutron Cross Sections, vol. 2. Academic Press, San Diego.
- Neutron Detectors, 1966. International Atomic Energy Agency, Bibliographical Series, No. 18, Vienna.
- Schulte, R.L., Swanson, F., Kesselman, M., 1994. The use of large area silicon sensors for thermal neutron detection. Nuclear Instruments and Methods A 353, 123–127.
- Shultis, J.K., Faw, R.E., 2000. Radiation Shielding. American Nuclear Society, La Grange Park, IL.
- Shultis, J.K., McGregor, D.S., 2006. Efficiencies of coated and perforated semiconductor neutron detectors. IEEE Transactions on Nuclear Science 53, 1659–1665.
- Ziegler, J.F., Biersack, J.P., 2003. Transport of ions in matter in SRIM-2003 code, version 26 (www.srim.org) (IBM Corp., 2003).